Development of a harmonic balance method-based numerical strategy for blade-tip/casing interactions: application to NASA rotor 37

Yann Colaïtis, Alain Batailly

POLYTECHNIQUE MONTRÉAL
UNIVERSITÉ D'INGÉNIERIE

LABORATOIRE D'ANALYSE VIBRATOIRE ET ACOUSTIQUE

Development of a harmonic balance method-based numerical strategy for blade-tip/casing interactions: application to NASA rotor 37

Y. Colaïtis[1], A. Batailly

Abstract

In this study, a frequency-domain approach based on the harmonic balance method coupled to a predictor-corrector continuation algorithm is implemented for the qualitative analysis of blade-tip/casing contacts in aircraft engines. Unilateral contact and dry friction are taken into account through a regularized penalty law. To enhance the robustness of the methodology, particular attention is paid to the mitigation of the Gibbs phenomenon. To this end, the employed Alternating Frequency/Time scheme features a Lanczos σ-approximation so that spurious oscillations of the computed nonlinear contact forces become negligible. This approach is applied in combination with a model reduction technique on an industrial compressor blade: NASA rotor 37. In order to assess the influence of both the contact law regularization and the Lanczos σ-approximation, obtained results are thoroughly compared to an existing time integration-based numerical strategy relying on a Lagrange multiplier-based approach for contact treatment and that was previously confronted to experimental results. Presented results underline the very good agreement between the proposed methodology and the reference time integration numerical strategy. The proposed developments thus complement existing results on blade-tip/casing contact adding a much needed qualitative understanding of the interaction and an accurate assessment of the contact stiffening phenomenon.

Keywords

harmonic balance method; numerical continuation; blade-tip/casing contacts; rotor/stator interaction; compressor blade

1 - Department of Mechanical Engineering, École Polytechnique de Montréal, P.O. Box 6079, Succ. Centre-Ville, Montréal, Québec, Canada H3C 3A7

Développement d'une stratégie numérique basée sur la méthode de l'équilibrage harmonique pour les interactions aubes/carter : application au rotor 37 de la NASA

Y. Colaïtis[1], A. Batailly

Résumé

Dans cette étude, une approche fréquentielle basée sur la méthode de l'équilibrage harmonique couplée à un algorithme de continuation de logique prédicteur-correcteur est mise en œuvre pour l'analyse qualitative des contacts aubes/carter dans les moteurs d'avion. Le contact unilatéral et le frottement sec sont pris en compte par une loi de pénalité régularisée. Pour renforcer la robustesse de la méthodologie, une attention particulière est accordée à l'atténuation du phénomène Gibbs. Dans ce but, le schéma d'Alternance Fréquence/Temps employé comporte une approximation σ de Lanczos de sorte que les oscillations parasites générées dans les efforts de contact non-linéaires calculées deviennent négligeables. Cette approche est appliquée en conjonction d'une technique de réduction de modèle sur une aube de compresseur industriel : le rotor 37 de la NASA. Afin d'évaluer l'influence de la régularisation de la loi de contact et de l'approximation de Lanczos, les résultats obtenus sont comparés de manière approfondie à une stratégie numérique existante basée sur de l'intégration temporelle qui repose sur une approche basée sur le multiplicateur de Lagrange pour le traitement des contacts, et qui a été confrontée par le passé à des résultats expérimentaux. Les résultats présentés soulignent un accord très satisfaisant entre la méthodologie proposée et la stratégie numérique d'intégration temporel de référence. Les développements proposés complémentent donc les résultats déjà existants sur le contact aubes/carter en permettant notamment d'offrir une compréhension qualitative indispensable de l'interaction ainsi qu'une évaluation précise du phénomène de raidissement du contact.

Mots-clés

méthode de l'équilibrage harmonique; continuation numérique; contacts aube/carter; interactions rotor/stator; aube de compresseur

1 - Département de génie mécanique, École Polytechnique de Montréal, P.O. Box 6079, Succ. Centre-Ville, Montréal, Québec, Canada H3C 3A7

1 Introduction

In order to maximize an aircraft engine's efficiency and reduce its environmental footprint, designers focus on using new lighter materials as well as reducing operating clearances [1], particularly within compressor stages. The latter unavoidably implies more frequent structural contacts between rotating components and their surrounding casings, to a point where these contact events must now be accounted for in non-accidental configurations [2]. Should these contact events occur in a stage where new and lighter materials are used—such as a turbine stage for instance—, designers face a new challenge: these contacts may indeed yield stress levels detrimental to the impacted components, since these new materials feature notably lower admissible stresses than their titanium alloys counterpart [3]. In this context, there is a critical need for designers to accurately predict blade-tip/casing contacts and related interactions.

Over the past decade, numerical time integration has been the workhorse of researchers interested in the prediction of blade-tip/casing contacts in aircraft engines [4, 5]. While this choice implied costly numerical simulations in terms of computation times, it was motivated by several specific factors. Firstly, considering the relatively low incursion rates of blades within the casing and the very high relative speeds between the two components, it was assumed that a very accurate contact treatment algorithm was essential to obtain physically relevant results [6], including a valid estimate of the contact stiffening phenomenon. This observation led several researchers to favor numerical time integration over frequency-domain methodologies since the former easily allows to implement a variety of contact algorithms. Secondly, conclusions drawn from published experimental studies put forward that witnessed interactions are often related to transient or diverging motions which may not be captured with frequency-domain approaches. Thirdly, while frequency-domain approaches are often viewed as more computationally efficient than time integration methods, they still represent a computational challenge when applied to complex mechanical systems with a large number of nonlinear degrees of freedom (dof), even more so when one of the two impacting structures is assumed to be perfectly rigid [7]. For all these reasons, most of the published numerical work that was compared to experimental observations relied on time integration methods.

While numerical time integration has demonstrated its potential for the prediction of experimentally observed interactions, it is also patent that it is intrinsically limited to quantitative results. Gaining a qualitative understanding of blade-tip/casing contacts with numerical time integration would indeed require a potentially infinite number of simulations. Thus, there is a need for another solution paradigm that could provide this qualitative understanding of the investigated problem.

Among the frequency domain approaches that are available in the literature, the Harmonic Balance Method (HBM) became increasingly popular in the field of turbomachinery over the past fifteen years. In particular, it has been successfully used for the prediction of shaft/bearing interactions [8, **?**] and the simulation of blade friction damping [9, 10, 11]. Its use for the blade-tip/casing interface remains however very limited [12] due to the numerical severity of the associated contact problem. The sensitivity of the HBM to the well-known Gibbs phenomenon [13] has been underlined by many researchers as a roadblock for the application of this method to blade-tip/casing contacts [7].

In this paper, a modified HBM-based methodology featuring both a regularized contact law and a dedicated filtering technique is presented and applied for the prediction of blade-tip/casing contacts. The second section of the paper is centered on a detailed presentation of the proposed methodology. The third section then focuses on the investigated contact case study, including the presentation of the open blade model based on NASA rotor 37. Finally, in the fourth section, results obtained with the proposed methodology are thoroughly validated with respect to a reference time-integration based numerical strategy.

2 Regularized-Lanczos harmonic balance

The equation of motion of a n-dof nonlinear mechanical system reads:

$$\mathbf{M}\ddot{\boldsymbol{x}} + \mathbf{C}\dot{\boldsymbol{x}} + \mathbf{K}\boldsymbol{x} + \boldsymbol{f}_{\mathrm{nl}}(\boldsymbol{x}, \dot{\boldsymbol{x}}) = \boldsymbol{f}_{\mathrm{ext}}(\omega, t) \tag{1}$$

where $\mathbf{M}$, $\mathbf{C}$, $\mathbf{K}$ are the mass, damping and stiffness matrices, $\boldsymbol{x}$ is the displacement vector, $\boldsymbol{f}_{\mathrm{nl}}$ is the nonlinear forces and $\boldsymbol{f}_{\mathrm{ext}}$ corresponds to the periodic excitation forces of angular frequency ω. The overdots refer to derivatives with respect to time t.

2.1 The Harmonic Balance Method

The HBM relies on the assumption that the solutions of Eq. (1) $\boldsymbol{x}$ may be expressed as H-truncated Fourier series:

$$\boldsymbol{x}(t) \simeq \frac{1}{2}\boldsymbol{a}_0 + \sum_{j=1}^{H} \left[\boldsymbol{a}_j \cos\left(j\omega t\right) + \boldsymbol{b}_j \sin\left(j\omega t\right)\right] \tag{2}$$

where vectorial quantities $\boldsymbol{a}_j$ are the unknown real Fourier coefficients respectively related to cosine terms and $\boldsymbol{b}_j$ the ones related to sine terms. Each of these coefficients are defined as follows:

$$\begin{cases} \boldsymbol{a}_j = \left[a_j^1,\, a_j^2,\, \ldots,\, a_j^n\right] & \text{for } j \in [\![0..H]\!] \\ \boldsymbol{b}_j = \left[b_j^1,\, b_j^2,\, \ldots,\, b_j^n\right] & \text{for } j \in [\![1..H]\!] \end{cases} \tag{3}$$

The same spectral decomposition is also applied to forces $\boldsymbol{f}_{\text{nl}}$ and $\boldsymbol{f}_{\text{ext}}$. For the sake of clarity, all Fourier coefficients are gathered in $n(2H+1)$-dimensional vectors resulting in the following frequency-domain variables:

$$\begin{aligned} \tilde{\boldsymbol{x}} &= \left[\,\boldsymbol{a}_0,\, \boldsymbol{a}_1,\, \boldsymbol{b}_1,\, \ldots,\, \boldsymbol{a}_H,\, \boldsymbol{b}_H\,\right]^\top \\ \tilde{\boldsymbol{f}}_{\text{nl}} &= \left[\,\boldsymbol{a}_0^{\text{nl}},\, \boldsymbol{a}_1^{\text{nl}},\, \boldsymbol{b}_1^{\text{nl}},\, \ldots,\, \boldsymbol{a}_H^{\text{nl}},\, \boldsymbol{b}_H^{\text{nl}}\,\right]^\top \\ \tilde{\boldsymbol{f}}_{\text{ext}} &= \left[\,\boldsymbol{a}_0^{\text{ext}},\, \boldsymbol{a}_1^{\text{ext}},\, \boldsymbol{b}_1^{\text{ext}},\, \ldots,\, \boldsymbol{a}_H^{\text{ext}},\, \boldsymbol{b}_H^{\text{ext}}\,\right]^\top \end{aligned} \tag{4}$$

From that point, displacements vector $\boldsymbol{x}(t)$ of Eq. (2), its derivatives, $\dot{\boldsymbol{x}}(t)$ and $\ddot{\boldsymbol{x}}(t)$, as well as forces, are substituted into Eq. (1). A Fourier-Galerkin projection [14] then yields $n(2H+1)$ nonlinear algebraic equations in the frequency domain:

$$\mathbf{R}(\tilde{\boldsymbol{x}}, \omega) = \mathbf{Z}(\omega)\tilde{\boldsymbol{x}} + \tilde{\boldsymbol{f}}_{\text{nl}}(\tilde{\boldsymbol{x}}) - \tilde{\boldsymbol{f}}_{\text{ext}}(\omega) = \mathbf{0} \tag{5}$$

where $\mathbf{Z}(\omega)$ is the dynamic stiffness matrix, a block diagonal matrix which characterizes the linear dynamics of the response of the system and is defined as follows:

$$\mathbf{Z}(\omega) = \omega^2 \boldsymbol{\nabla}^2 \otimes \mathbf{M} + \omega \boldsymbol{\nabla} \otimes \mathbf{C} + \mathbf{I}_{2H+1} \otimes \mathbf{K} \tag{6}$$

where $\otimes$ denotes the Kronecker product and $\mathbf{I}_{2H+1}$ is the identity matrix of size $2H+1$. The matrix $\boldsymbol{\nabla}$ corresponds to a frequency-domain differential operator, *i.e.* within Fourier trigonometrical basis, and is defined by:

$$\boldsymbol{\nabla} = \text{diagblock}(0,\, \boldsymbol{\nabla}_1,\, \ldots,\, \boldsymbol{\nabla}_j,\, \ldots,\, \boldsymbol{\nabla}_H) \quad \text{and} \quad \boldsymbol{\nabla}^2 = \boldsymbol{\nabla}\boldsymbol{\nabla} \tag{7}$$

with the elementary first order derivative matrix $\boldsymbol{\nabla}_j$:

$$\boldsymbol{\nabla}_j = j \begin{bmatrix} 0 & 1 \\ -1 & 0 \end{bmatrix} \text{ for } j \in [\![1..H]\!] \tag{8}$$

Solutions of Eq. (5) may be obtained using a Newton-Raphson algorithm. Starting from a proper initial guess $\tilde{\boldsymbol{x}}^0$, a converged solution is obtained iteratively:

$$\tilde{\boldsymbol{x}}^{k+1} = \tilde{\boldsymbol{x}}^k + \Delta\tilde{\boldsymbol{x}}^k \quad \text{with} \quad \mathbf{R}^k_{,\tilde{\boldsymbol{x}}} \Delta\tilde{\boldsymbol{x}}^k = -\mathbf{R}^k \tag{9}$$

where $\mathbf{R}^k = \mathbf{R}(\tilde{\boldsymbol{x}}^k, \omega)$ is the residual at iteration k and $\mathbf{R}^k_{,\tilde{\boldsymbol{x}}}$ is the jacobian matrix of the system with respect to $\tilde{\boldsymbol{x}}^k$:

$$\mathbf{R}^k_{,\tilde{\boldsymbol{x}}} = \frac{\partial \mathbf{R}}{\partial \tilde{\boldsymbol{x}}}(\tilde{\boldsymbol{x}}^k, \omega) = \mathbf{Z}(\omega) + \tilde{\boldsymbol{f}}_{\text{nl},\tilde{\boldsymbol{x}}} = \mathbf{Z}(\omega) + \frac{\partial \tilde{\boldsymbol{f}}_{\text{nl}}(\tilde{\boldsymbol{x}}^k)}{\partial \tilde{\boldsymbol{x}}} \tag{10}$$

Iterations are stopped once a relative error convergence criterion has been satisfied.

2.2 Path following: continuation

Amplitude jumps are often to be expected during frequency sweeps of nonlinear mechanical systems. These phenomena are a clear indication that coexisting stable solutions may exist for a given angular frequency ω. By coupling it to a continuation technique [8], the HBM becomes well-suited for the prediction of such coexisting solutions.

From the implicit function theorem, it comes that the solution set of Eq. (5) can be locally parameterized. Continuation techniques are built upon this mathematical property and thus take advantage of the fact that the computation of a solution of the system at a given angular frequency ω may reasonably be obtained from solutions previously computed in the vicinity of ω. Among the available continuation techniques in the literature [8, 15], the arc-length continuation technique may be the most commonly used and is also considered in this paper.

Predictor-corrector continuation techniques are characterized by three key elements: parameterization, prediction step, and correction step.

Parameterization

The arc-length continuation technique relates to parameterization of the Nonlinear Frequency Response Curve (NFRC) with respect to the arc-length parameter s (also often referred to as the curvilinear abscissa of the NFRC). When solving Eq. (5), Newton's direction is therefore constrained by the following parameterization $\mathcal{P}$:

$$\mathcal{P}(\tilde{\boldsymbol{x}}_{i+1}^k, \omega_{i+1}^k, s) = ||\tilde{\boldsymbol{x}}_{i+1}^k - \tilde{\boldsymbol{x}}_i||_2^2 + (\omega_{i+1}^k - \omega_i)^2 - \Delta s_{i+1}^2 = 0 \tag{11}$$

As ω becomes an additional unknown, the size of the system to solve in Eq. (5) is increased and the unknown vector now reads: $\boldsymbol{y}_{i+1} = [\tilde{\boldsymbol{x}}_{i+1}, \omega_{i+1}]^\top$.

Prediction step

In order to initiate the iterative correction procedure and enhance the chances of a successful convergence, a prediction is first made. A secant predictor is here used as it was found to enhance the robustness of the methodology when considering contact nonlinearities. The predicted solution $\boldsymbol{y}_{i+1}^0$ is computed using the last two found solutions $\boldsymbol{y}_{i-1}$ and $\boldsymbol{y}_i$ and is located at a distance Δs_{i+1} along the normalized secant direction:

$$\boldsymbol{y}_{i+1}^0 = \boldsymbol{y}_i + \Delta s_{i+1} \frac{\boldsymbol{y}_i - \boldsymbol{y}_{i-1}}{||\boldsymbol{y}_i - \boldsymbol{y}_{i-1}||_2} \tag{12}$$

Correction step

This last step should be interpreted as enforcing the point $\boldsymbol{y}_{i+1}^k$ to lie at the intersection of the residual curve $\mathbf{R}(\tilde{\boldsymbol{x}}, \omega) = \mathbf{0}$ and the surface of an hypersphere of radius Δs centered on the previous solution $\boldsymbol{y}_i$. Newton-Raphson subsequent corrections are then obtained by solving the augmented system:

$$\begin{bmatrix} \mathbf{R}_{,\tilde{\boldsymbol{x}}}(\boldsymbol{y}_{i+1}^k) & \mathbf{R}_{,\omega}(\boldsymbol{y}_{i+1}^k) \\ \mathcal{P}_{,\tilde{\boldsymbol{x}}}^\top(\boldsymbol{y}_{i+1}^k, s) & \mathcal{P}_{,\omega}(\boldsymbol{y}_{i+1}^k, s) \end{bmatrix} \begin{bmatrix} \Delta\tilde{\boldsymbol{x}} \\ \Delta\omega \end{bmatrix} = \begin{bmatrix} -\mathbf{R}(\boldsymbol{y}_{i+1}^k) \\ -\mathcal{P}(\boldsymbol{y}_{i+1}^k, s) \end{bmatrix} \tag{13}$$

where $\mathcal{P}_{,\tilde{\boldsymbol{x}}}$ and $\mathcal{P}_{,\omega}$ refer to the partial derivatives of Eq. (11) with respect to $\tilde{\boldsymbol{x}}$ and ω, and where $\mathbf{R}_{,\omega}$ is the gradient of system (5) with respect to ω is given by:

$$\mathbf{R}_{,\omega} = \mathbf{Z}_{,\omega}\tilde{\boldsymbol{x}} + \tilde{\boldsymbol{f}}_{\mathrm{nl},\omega} - \tilde{\boldsymbol{f}}_{\mathrm{ext},\omega} = \left(2\omega\boldsymbol{\nabla}^2 \otimes \mathbf{M} + \boldsymbol{\nabla} \otimes \mathbf{C}\right)\tilde{\boldsymbol{x}} + \tilde{\boldsymbol{f}}_{\mathrm{nl},\omega} - \tilde{\boldsymbol{f}}_{\mathrm{ext},\omega} \tag{14}$$

Numerical considerations

By noticing the bordered structure of the augmented jacobian matrix in Eq. (13), this system may be advantageously solved using a block elimination algorithm [16]. This technique prevents numerical difficulties that may arise from the singularity of the jacobian matrix $\mathbf{R}_{,\tilde{\boldsymbol{x}}}$ at turning points. Besides, it allows factorizing only $\mathbf{R}_{,\tilde{\boldsymbol{x}}}$, which is done with a partially pivoted LU decomposition.

2.3 Computation of nonlinear contact forces

Alternating Frequency/Time scheme

Eventhough the expression of the external forcing $\tilde{\boldsymbol{f}}_{\text{ext}}$ is usually known, it is generally not possible to have an explicit analytical expression of the nonlinear forces $\tilde{\boldsymbol{f}}_{\text{nl}}$. As a consequence, an Alternating Frequency/Time (AFT) scheme [17] may be used to address this issue. The AFT scheme consists in using inverse an Discrete Fourier Transform (DFT) to evaluate in the time domain the expression of nonlinear forces $\boldsymbol{f}_{\text{nl}}(\boldsymbol{x}, \dot{\boldsymbol{x}})$ and their partial derivatives $\boldsymbol{f}_{\text{nl},\boldsymbol{x}}$, $\boldsymbol{f}_{\text{nl},\dot{\boldsymbol{x}}}$ and $\boldsymbol{f}_{\text{nl},\omega}$. These terms are then projected back onto the frequency domain using a forward DFT to obtain $\tilde{\boldsymbol{f}}_{\text{nl}}$, $\tilde{\boldsymbol{f}}_{\text{nl},\tilde{\boldsymbol{x}}}$ and $\tilde{\boldsymbol{f}}_{\text{nl},\omega}$.

In the time domain, $\boldsymbol{x}$ and $\boldsymbol{f}_{\text{nl}}$ are evaluated at N evenly distributed time steps over one period T, $t_i = \frac{2\pi}{\omega}\frac{i}{N}$ for $i \in [\![0..N-1]\!]$, so that:

$$\begin{aligned} \boldsymbol{x} &= [\boldsymbol{x}_1, \dots, \boldsymbol{x}_n]^\top = [x_{1,0}, \dots, x_{1,N-1}, \dots, x_{n,0}, \dots, x_{n,N-1}]^\top \\ \boldsymbol{f}_{\text{nl}}(\boldsymbol{x}, \dot{\boldsymbol{x}}) &= [\boldsymbol{f}_1, \dots, \boldsymbol{f}_n]^\top = [f_{1,0}, \dots, f_{1,N-1}, \dots, f_{n,0}, \dots, f_{n,N-1}]^\top \end{aligned} \tag{15}$$

One may note that, for the sake of readability, subscript nl has been dropped for vectors and matrices related to nonlinear force terms. Displacement, velocity and acceleration fields in the time domain may then be obtained using inverse DFT [18]:

$$\boldsymbol{x} = \boldsymbol{\Gamma}\tilde{\boldsymbol{x}}, \quad \dot{\boldsymbol{x}} = \omega\boldsymbol{\Gamma}(\boldsymbol{\nabla} \otimes \mathbf{I}_n)\tilde{\boldsymbol{x}}, \quad \text{and} \quad \ddot{\boldsymbol{x}} = \omega^2\boldsymbol{\Gamma}(\boldsymbol{\nabla}^2 \otimes \mathbf{I}_n)\tilde{\boldsymbol{x}} \tag{16}$$

with $\boldsymbol{\Gamma}$, the rectangular $(nN \times n(2H+1))$-dimensional inverse DFT matrix:

$$\begin{aligned} \boldsymbol{\Gamma} = \Bigg[\mathbf{I}_n \otimes \begin{bmatrix} 1/2 \\ \vdots \\ 1/2 \end{bmatrix} \mathbf{I}_n \otimes \begin{bmatrix} \cos(\omega t_0) \\ \vdots \\ \cos(\omega t_{N-1}) \end{bmatrix} \mathbf{I}_n \otimes \begin{bmatrix} \sin(\omega t_0) \\ \vdots \\ \sin(\omega t_{N-1}) \end{bmatrix} \dots \\ \dots \quad \mathbf{I}_n \otimes \begin{bmatrix} \cos(H\omega t_0) \\ \vdots \\ \cos(H\omega t_{N-1}) \end{bmatrix} \quad \mathbf{I}_n \otimes \begin{bmatrix} \sin(H\omega t_0) \\ \vdots \\ \sin(H\omega t_{N-1}) \end{bmatrix} \Bigg] \end{aligned} \tag{17}$$

Conversely, frequency domain quantities may be obtained from their time domain counterparts through a DFT:

$$\tilde{\boldsymbol{x}} = \boldsymbol{\Gamma}^{-1}\boldsymbol{x}, \quad \text{and} \quad \tilde{\boldsymbol{f}}_{\text{nl}} = \boldsymbol{\Gamma}^{-1}\boldsymbol{f}_{\text{nl}} \tag{18}$$

where inverse $\boldsymbol{\Gamma}^{-1}$ is the forward DFT matrix and may be constructed in a similar fashion to $\boldsymbol{\Gamma}$, see [18].

By introducing the nondimensional time $\tau = \omega t$—or, in a discretized manner, $\tau_i = 2\pi\frac{i}{N}$ for $i \in [\![0..N-1]\!]$—in the operators $\boldsymbol{\Gamma}$ and $\boldsymbol{\Gamma}^{-1}$, the latter become advantageously independent of the angular frequency ω. This way, it is only required to evaluate these operators once, consequently yielding significant gains in terms of computational efficiency.

Semi-analytical computation of derivatives

Both the accuracy and the efficiency of the AFT procedure are highly dependent on the retained number of time steps N. While the Nyquist-Shanon criterion gives a theoretical lower bound value of N to prevent aliasing errors, *i.e.* $N \geq 2H+1$, when considering strong nonlinearities such as those related to structural contact, the AFT scheme often requires a much larger number of time samples [15]. That is why, a precise evaluation of the derivatives $\tilde{\boldsymbol{f}}_{\text{nl},\tilde{\boldsymbol{x}}}$ and $\tilde{\boldsymbol{f}}_{\text{nl},\omega}$ is crucial to ensure the robustness of any gradient based nonlinear solvers such as the Newton-Raphson method. Thereupon, the effectiveness of the AFT scheme is closely related to the derivation of the nonlinear forces [19]. The linearity of DFT operators $\boldsymbol{\Gamma}$ and $\boldsymbol{\Gamma}^{-1}$ along with the chain rule provide an efficient general analytic formulation of derivatives [11]:

$$\frac{\partial\tilde{\boldsymbol{f}}_{\text{nl}}(\tilde{\boldsymbol{x}})}{\partial\tilde{\boldsymbol{x}}} = \frac{\partial\tilde{\boldsymbol{f}}_{\text{nl}}}{\partial\boldsymbol{f}_{\text{nl}}}\frac{\partial\boldsymbol{f}_{\text{nl}}}{\partial\boldsymbol{x}}\frac{\partial\boldsymbol{x}}{\partial\tilde{\boldsymbol{x}}} + \frac{\partial\tilde{\boldsymbol{f}}_{\text{nl}}}{\partial\boldsymbol{f}_{\text{nl}}}\frac{\partial\boldsymbol{f}_{\text{nl}}}{\partial\dot{\boldsymbol{x}}}\frac{\partial\dot{\boldsymbol{x}}}{\partial\tilde{\boldsymbol{x}}} = \boldsymbol{\Gamma}^{-1}\frac{\partial\boldsymbol{f}_{\text{nl}}}{\partial\boldsymbol{x}}\boldsymbol{\Gamma} + \boldsymbol{\Gamma}^{-1}\frac{\partial\boldsymbol{f}_{\text{nl}}}{\partial\dot{\boldsymbol{x}}}\boldsymbol{\Gamma}(\omega\boldsymbol{\nabla} \otimes \mathbf{I}_n) \tag{19}$$

where the $(nN \times nN)$ matrices of partial derivatives of $\boldsymbol{f}_{\mathrm{nl}}$ evaluated at N time steps are defined by:

$$\frac{\partial \boldsymbol{f}_{\mathrm{nl}}}{\partial \boldsymbol{x}} = \begin{bmatrix} \mathrm{diag}\left(\frac{\partial \boldsymbol{f}_1}{\partial \boldsymbol{x}_1}\right) & \dots & \mathrm{diag}\left(\frac{\partial \boldsymbol{f}_1}{\partial \boldsymbol{x}_n}\right) \\ \vdots & \ddots & \vdots \\ \mathrm{diag}\left(\frac{\partial \boldsymbol{f}_n}{\partial \boldsymbol{x}_1}\right) & \dots & \mathrm{diag}\left(\frac{\partial \boldsymbol{f}_n}{\partial \boldsymbol{x}_n}\right) \end{bmatrix} \quad \text{and} \quad \frac{\partial \boldsymbol{f}_{\mathrm{nl}}}{\partial \dot{\boldsymbol{x}}} = \begin{bmatrix} \mathrm{diag}\left(\frac{\partial \boldsymbol{f}_1}{\partial \dot{\boldsymbol{x}}_1}\right) & \dots & \mathrm{diag}\left(\frac{\partial \boldsymbol{f}_1}{\partial \dot{\boldsymbol{x}}_n}\right) \\ \vdots & \ddots & \vdots \\ \mathrm{diag}\left(\frac{\partial \boldsymbol{f}_n}{\partial \dot{\boldsymbol{x}}_1}\right) & \dots & \mathrm{diag}\left(\frac{\partial \boldsymbol{f}_n}{\partial \dot{\boldsymbol{x}}_n}\right) \end{bmatrix}, \tag{20}$$

and where:

$$\frac{\partial \tilde{\boldsymbol{f}}_{\mathrm{nl}}(\tilde{\boldsymbol{x}}, \omega)}{\partial \omega} = \frac{\partial \tilde{\boldsymbol{f}}_{\mathrm{nl}}}{\partial \boldsymbol{f}_{\mathrm{nl}}} \frac{\partial \boldsymbol{f}_{\mathrm{nl}}}{\partial \omega} + \frac{\partial \tilde{\boldsymbol{f}}_{\mathrm{nl}}}{\partial \boldsymbol{f}_{\mathrm{nl}}} \frac{\partial \boldsymbol{f}_{\mathrm{nl}}}{\partial \dot{\boldsymbol{x}}} \frac{\partial \dot{\boldsymbol{x}}}{\partial \omega} = \boldsymbol{\Gamma}^{-1} \frac{\partial \boldsymbol{f}_{\mathrm{nl}}}{\partial \omega} + \boldsymbol{\Gamma}^{-1} \frac{\partial \boldsymbol{f}_{\mathrm{nl}}}{\partial \dot{\boldsymbol{x}}} \boldsymbol{\Gamma}(\boldsymbol{\nabla} \otimes \mathbf{I}_n) \tilde{\boldsymbol{x}} \tag{21}$$

2.4 Nonlinear condensation

For large industrial systems featuring nonlinear interfaces, it is common practice to distinguish the linear dof $\tilde{\boldsymbol{x}}^{\mathrm{l}}$ from the nonlinear dof $\tilde{\boldsymbol{x}}^{\mathrm{nl}}$ over which structural contacts may occur. This yields a a reorganization [20] of Eq. (5) which may then be written as:

$$\begin{bmatrix} \mathbf{Z}^{\mathrm{ll}} & \mathbf{Z}^{\mathrm{lnl}} \\ \mathbf{Z}^{\mathrm{nll}} & \mathbf{Z}^{\mathrm{nlnl}} \end{bmatrix} \begin{bmatrix} \tilde{\boldsymbol{x}}^{\mathrm{l}} \\ \tilde{\boldsymbol{x}}^{\mathrm{nl}} \end{bmatrix} + \begin{bmatrix} \tilde{\boldsymbol{f}}^{\mathrm{l}}_{\mathrm{nl}}(\tilde{\boldsymbol{x}}^{\mathrm{nl}}) \\ \tilde{\boldsymbol{f}}^{\mathrm{nl}}_{\mathrm{nl}}(\tilde{\boldsymbol{x}}^{\mathrm{nl}}) \end{bmatrix} - \begin{bmatrix} \tilde{\boldsymbol{f}}^{\mathrm{l}}_{\mathrm{ext}} \\ \tilde{\boldsymbol{f}}^{\mathrm{nl}}_{\mathrm{ext}} \end{bmatrix} = \mathbf{0} \tag{22}$$

The first line of Eq. (22) leads to the expression of the linear dof $\tilde{\boldsymbol{x}}^{\mathrm{l}}$ as a function of the nonlinear dof $\tilde{\boldsymbol{x}}^{\mathrm{nl}}$:

$$\tilde{\boldsymbol{x}}^{\mathrm{l}} = \mathbf{Z}^{\mathrm{ll}^{-1}} \left[\tilde{\boldsymbol{f}}^{\mathrm{l}}_{\mathrm{ext}} - \mathbf{Z}^{\mathrm{lnl}} \tilde{\boldsymbol{x}}^{\mathrm{nl}} - \tilde{\boldsymbol{f}}^{\mathrm{l}}_{\mathrm{nl}}(\tilde{\boldsymbol{x}}^{\mathrm{nl}})\right] \tag{23}$$

which may be used in the second line of Eq. (22) to reduce the dimension of the system to that of the nonlinear dof $\tilde{\boldsymbol{x}}^{\mathrm{nl}}$:

$$\left[\mathbf{Z}^{\mathrm{nlnl}} - \mathbf{Z}^{\mathrm{nll}} \mathbf{Z}^{\mathrm{ll}^{-1}} \mathbf{Z}^{\mathrm{lnl}}\right] \tilde{\boldsymbol{x}}^{\mathrm{nl}} + \left(\tilde{\boldsymbol{f}}^{\mathrm{nl}}_{\mathrm{nl}}(\tilde{\boldsymbol{x}}^{\mathrm{nl}}) - \mathbf{Z}^{\mathrm{nll}} \mathbf{Z}^{\mathrm{ll}^{-1}} \tilde{\boldsymbol{f}}^{\mathrm{l}}_{\mathrm{nl}}(\tilde{\boldsymbol{x}}^{\mathrm{nl}})\right) - \left(\tilde{\boldsymbol{f}}^{\mathrm{nl}}_{\mathrm{ext}} - \mathbf{Z}^{\mathrm{nll}} \mathbf{Z}^{\mathrm{ll}^{-1}} \tilde{\boldsymbol{f}}^{\mathrm{l}}_{\mathrm{ext}}\right) = \mathbf{0} \tag{24}$$

or, in a more compact form:

$$\mathbf{Z}_{\mathrm{red}} \tilde{\boldsymbol{x}}^{\mathrm{nl}} + \tilde{\boldsymbol{f}}_{\mathrm{nl,red}}(\tilde{\boldsymbol{x}}^{\mathrm{nl}}) - \tilde{\boldsymbol{f}}_{\mathrm{ext,red}} = \mathbf{0} \tag{25}$$

Considering Eq. (25), the gradient $\mathbf{R}_{,\omega}$ from Eq. (14) is now expressed as:

$$\mathbf{R}_{,\omega} = \mathbf{Z}_{\mathrm{red},\omega} \tilde{\boldsymbol{x}}^{\mathrm{nl}} + \tilde{\boldsymbol{f}}_{\mathrm{nl,red},\omega} - \tilde{\boldsymbol{f}}_{\mathrm{ext,red},\omega} \tag{26}$$

with:

$$\mathbf{Z}_{\mathrm{red},\omega} = \mathbf{Z}^{\mathrm{nlnl}}_{,\omega} - \mathbf{Z}^{\mathrm{nll}}_{,\omega} \mathbf{Z}^{\mathrm{ll}^{-1}} \mathbf{Z}^{\mathrm{lnl}} - \mathbf{Z}^{\mathrm{nll}} \left[\mathbf{Z}^{\mathrm{ll}^{-1}}\right]_{,\omega} \mathbf{Z}^{\mathrm{lnl}} - \mathbf{Z}^{\mathrm{nll}} \mathbf{Z}^{\mathrm{ll}^{-1}} \mathbf{Z}^{\mathrm{lnl}}_{,\omega} \tag{27}$$

and:

$$\tilde{\boldsymbol{f}}_{\mathrm{ext,red},\omega} = \frac{\partial \tilde{\boldsymbol{f}}^{\mathrm{nl}}_{\mathrm{ext}}}{\partial \omega} - \mathbf{Z}^{\mathrm{nll}}_{,\omega} \mathbf{Z}^{\mathrm{ll}^{-1}} \tilde{\boldsymbol{f}}^{\mathrm{l}}_{\mathrm{ext}} - \mathbf{Z}^{\mathrm{nll}} \left[\mathbf{Z}^{\mathrm{ll}^{-1}}\right]_{,\omega} \tilde{\boldsymbol{f}}^{\mathrm{l}}_{\mathrm{ext}} - \mathbf{Z}^{\mathrm{nll}} \mathbf{Z}^{\mathrm{ll}^{-1}} \frac{\partial \tilde{\boldsymbol{f}}^{\mathrm{l}}_{\mathrm{ext}}}{\partial \omega} \tag{28}$$

where the derivative with respect to ω of the inverse $\mathbf{Z}^{\mathrm{ll}^{-1}}$ is obtained through the formula $[\mathbf{Z}^{\mathrm{ll}^{-1}}]_{,\omega} = -\mathbf{Z}^{\mathrm{ll}^{-1}} \mathbf{Z}^{\mathrm{ll}}_{,\omega} \mathbf{Z}^{\mathrm{ll}^{-1}}$. Lastly, given the assumption that $\tilde{\boldsymbol{f}}^{\mathrm{l}}_{\mathrm{nl}}(\tilde{\boldsymbol{x}}^{\mathrm{nl}}) = \mathbf{0}$, the reduced gradient $\tilde{\boldsymbol{f}}_{\mathrm{nl,red},\omega}$ remains equal to the one in Eq. (21).

2.5 Specific developments for blade-tip/casing contact

The aforementioned developments are recalled for the sake of completeness as they have already been widely used in the literature [14] for various types of nonlinearities. Nonetheless, when considering the HBM with contacts nonlinearities, it has been shown that it is prone to the Gibbs phenomenon [13] and, as a result, performs poorly [7].

The Gibbs phenomenon is related to the non-uniform convergence of Fourier series when approximating nonsmooth functions. It is evidenced by the overshoot or undershoot of the approximation where the approximated function is discontinuous thus yielding oscillations of the approximation. This phenomenon does not vanish when the number of harmonics is increased. Within the framework of the HBM, these spurious oscillations deteriorate the accuracy of the iterative procedure to a point that a converged solution may not be obtained. In this section, two key elements are presented to mitigate the Gibbs phenomenon: a regularized penalty law in order to smoothen contact management and a Lanczos filtering technique to prevent spurious oscillations on the displacements, velocities, and contact forces.

Regularized contact law

In the case of unilateral contact, normal contact forces $\boldsymbol{f}_{\mathrm{nl}}$ are deduced from constraint equations expressed by the Hertz-Signorini-Moreau conditions. Within the frequency methods' framework, several contact treatment algorithms have been developed to compute these forces including the augmented Lagrangian method [11] and the dynamic Lagrangian frequency time [9] approach. Another commonly used alternative is to employ a penalty formulation that directly allows one to compute the contact forces from the detected interpenetration of the structures. This latter approach is well-suited to the employed AFT scheme and is thus used in this paper.

The first step towards the computation of contact forces is the definition of the gap function $\boldsymbol{g}$ as the signed distance between contact nodes and an obstacle:

$$\boldsymbol{g}(t) = \boldsymbol{x}(t) - \boldsymbol{d}(t) \tag{29}$$

where $\boldsymbol{d}(t)$ refers to the time-dependent position of the obstacle. The penalty method consists in computing the normal component $\hat{\boldsymbol{f}}_{\mathrm{nl}}$ of the nonlinear forces as follows:

$$\hat{\boldsymbol{f}}_{\mathrm{nl}}(t) = \kappa \max\left(\boldsymbol{0}, \boldsymbol{g}(t)\right) \tag{30}$$

where $\kappa \in \mathbb{R}_+$ is the penalty coefficient and the max function provides a pairwise maximum of two vectors. The penalty coefficient must satisfy the following compromise: (1) on the one hand, it must be large enough to prevent non-negligible inter penetrations but, on the other hand, (2) considering too high values would yield an ill-conditioned numerical problem in Eq. (5).

In order to further enhance the robustness of the current approach, the activation function $\max\left(\boldsymbol{0}, \boldsymbol{g}(t)\right)$ of Eq. (30) is regularized [15], so that:

$$\hat{f}_{\mathrm{nl},j}(t) = \kappa \frac{g_j(t)}{2} + \sqrt{\left(\kappa \frac{g_j(t)}{2}\right)^2 + \gamma^2} \tag{31}$$

where $\gamma \in \mathbb{R}_+$ acts as a smoothing coefficient, and $\hat{f}_{\mathrm{nl},j}$ and g_j respectively refer to the coordinates of vectors $\hat{\boldsymbol{f}}_{\mathrm{nl}}$ and $\boldsymbol{g}$. It may be noted that Eqs. (30) and (31) are equivalent when $\gamma = 0$.

Filtering techniques

Even if the regularization of the contact law enhances the numerical robustness of the solver, it is found to have small impact on the Gibbs phenomenon. In order to mitigate this phenomenon, filtering techniques are here employed. One manifestation of the Gibbs phenomenon is that Fourier coefficients decay too slowly. For that reason, filtering techniques aim at altering these coefficients in order to make them decay faster. Classical filters include Fejér averaging, the raised cosine filter and its sharpened version, family of exponential filters and the second order Lanczos filter (also known as σ-approximation or Lanczos σ-averaging) [13]. Filtering can be shown as equivalent to introducing a decaying multiplicative factor σ_j to nonlinear forces $\boldsymbol{f}_{\mathrm{nl}}$ in Fourier space:

$$\boldsymbol{f}_{\mathrm{nl}}(\boldsymbol{x}, \dot{\boldsymbol{x}}) \simeq \frac{1}{2}\boldsymbol{a}_0^{\mathrm{nl}} + \sum_{j=1}^{H} \sigma_j \left[\boldsymbol{a}_j^{\mathrm{nl}} \cos\left(j\omega t\right) + \boldsymbol{b}_j^{\mathrm{nl}} \sin\left(j\omega t\right)\right] \tag{32}$$

where σ_j factors are defined as:

$$\sigma_j = \begin{cases} 1 - \mathcal{X}_j & \text{Fejér averaging} \\ \operatorname{sinc}(\mathcal{X}_j)^m & \text{Lanczos filter} \\ \frac{1}{2}(1 + \cos(\pi \mathcal{X}_j)) & \text{raised cosine filter} \end{cases} \tag{33}$$

where sinc is the normalized cardinal sine function and $m \in \mathbb{R}_+$ controls the smoothing intensity by allowing to carry out m consecutive Lanczos averagings [13, 21]. The parameter $\mathcal{X}_j$ allows to control the amount of filtering for each harmonic of the truncated Fourier series and is defined by:

$$\mathcal{X}_j = \begin{cases} 0 & \text{for } j < C_H \\ \frac{j}{H+1} & \text{for } C_H \leq j \leq H \end{cases} \tag{34}$$

where the cut-off harmonic C_H controls the onset of the filtering window. The effect of these filters is presented in Fig. 1 for a sawtooth wave. Fejér averaging has the particularity to totally curtail the overshoots and undershoots of

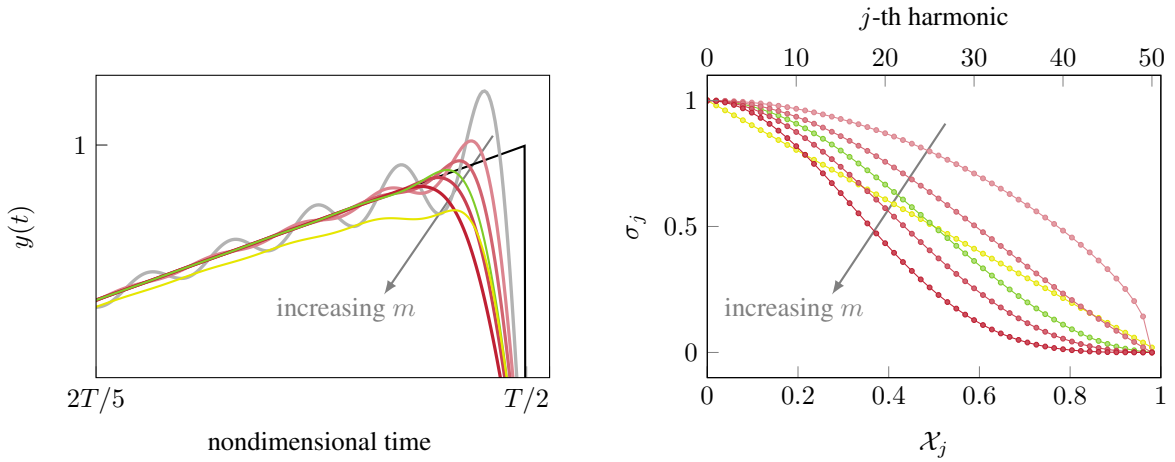

(a) Sawtooth wave (—), Fourier (—) and filtered series

(b) Filtering factors

Figure 1 – Filters: Fejér (—●—), Lanczos $m = 0.5$ (—●—), 1 (—●—), 2 (—●—), 3 (—●—) and raised cosine (—●—) ($H = 50$, $C_H = 0$).

the Gibbs phenomenon (due to the positivity of the Fejér kernel). Nevertheless, raised cosine and Lanczos filters still cut down the Gibbs phenomenon considerably and have better convergence near the discontinuities, *i.e.* a faster rising time which is key to better capture contact/no contact states transition.

In the context of the HBM, filtering is directly applied into the AFT cycle by ponderating each j-th harmonic of the forward DFT operator $\mathbf{\Gamma}^{-1}$ by its corresponding σ_j factor. It was found that the variation of filtering parameters did not significantly impact the results presented in the next section. Optimizing filtering parameters for this specific industrial application goes beyond the scope of this paper. Its purpose is to present an industry-ready frequency-domain approach for the qualitative analysis of blade-tip/casing interactions. Only unitary filters are considered, *i.e.* $m = C_H = 1$ (as in [21]).

3 Blade-tip/casing interaction on NASA rotor 37

Designed at NASA's Lewis research center in the late 1970s as part of aerodynamics research [22], rotor 37 is a 36-blade transonic axial compressor stage, see Fig. 2. It has been widely used in the field of Computed Fluid Dynamics (CFD) and notably served as a blind test case to assess the performance of CFD solvers in the 1990s. More

recently, a benchmark based on this blade was proposed for the analysis of blade-tip/casing contact interactions [23] and is used in this article.

3.1 Blade model

Rotor 37 is made of a nickel-based alloy: maraging steel grade 200. More specifically, the mechanical properties of a 18-Ni 200-maraging alloy are considered for the numerical simulations with a Young's modulus $E = 180$ GPa, a density $\rho = 8000$ kg·m^{-3} and a Poisson's ratio $\nu = 0.3$.

The 3D finite element model of the blade comprises 1800 quadratic hexahedral elements with 5745 nodes, it is depicted in Fig 2. The blade is clamped at its root. For numerical efficiency reasons, a reduced-order model is computed from the full finite element model by using the Craig-Bampton method [24] as it was shown to be well-suited for problems with contact nonlinearities [25]. The contact interface, also shown in Fig. 2, contains $n_b = 8$ boundary nodes, evenly spaced along the blade-tip. The resulting reduced order model contains 24 nonlinear dof and $\eta = 10$ modal dof thus yielding a total of 34 dof. Convergence of the blade eigenfrequencies for the first free vibration modes with respect to the discretization of the mesh as well as to the reduction parameter η was checked but is not detailed here for the sake of conciseness. Structural damping is represented by a modal damping, considering a coefficient $\xi = 1 \cdot 10^{-3}$ for the first bending and torsional modes, and $\xi = 5 \cdot 10^{-3}$ for all other modes.

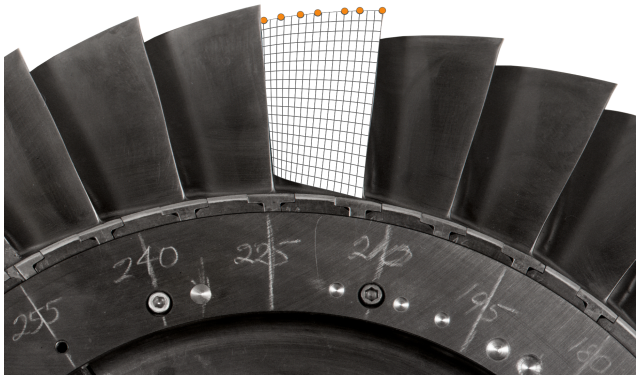

Figure 2 – Partial view of NASA rotor 37 [26] and finite element mesh with selected boundary nodes (●).

3.2 Contact scenario

Considering the fact that most blade-tip/casing experiments were carried out inside vacuum chambers [2], aerodynamic forcing is often disregarded for blade-tip/casing contact simulations, so that $\boldsymbol{f}_{\text{ext}}(\omega, t) = \mathbf{0}$. In addition, experimental observations repeatedly highlighted that the vibration amplitudes of the surrounding casing are negligible, which supports the assumption that it may be considered perfectly rigid. Within an aircraft engine, the initiation of contact between a blade and its surrounding casing are usually related to a displacement of the blade-tip due to centrifugal loads as the blade accelerates or a displacement of the casing under thermal loadings for instance. In the following, and in agreement with the benchmarck contact scenario with the same blade model [23], the casing is represented by a perfectly rigid mathematical profile. This profile is assumed to be distorted in such a way that there are two symmetrical privileged contact areas along the casing circumference. Because of this distortion, contacts occur at any angular speed.

3.3 Distorted casing

In the context of the HBM, the ovalized casing translates into a T-periodic distance function in Eq. (29). In agreement with the notations introduced in Eq. (15), it is denoted:

$$\boldsymbol{d} = [\boldsymbol{d}_1, \ldots, \boldsymbol{d}_{n_b}]^\top = [d_{1,0}, \ldots, d_{1,N-1}, \ldots, d_{n_b,0}, \ldots, d_{n_b,N-1}]^\top \tag{35}$$

where relative distance functions components are evaluated as follows:

$$d_{j,i} = c_j - (c_j + p_j) \exp\left[- \left(\frac{(\tau_i + \theta_j) \pmod{2\pi/n_l} - \pi/n_l}{w_l} \right)^2 \right] \tag{36}$$

for $j \in [\![1..n_b]\!]$, $i \in [\![0..N-1]\!]$ and where, n_l is the number of lobes, w_l is a weight parameter that defines the angular width of the contact areas along the casing circumference, θ_j is the angular shift of the j-th boundary node with respect to the reference position of the blade, c_j is the operating clearance and p_j defines the penetration of the casing profile with respect to the circle defined by the radial position of the j-th boundary node when the blade does not vibrate. The following values are considered in the remainder: $n_l = 2$, $w_l = 0.15$, and for all contact nodes, $c_j = 5 \cdot 10^{-4}$ m and $p_j = 1.25 \cdot 10^{-4}$ m. One lobe of the casing is illustrated in Fig. 3.

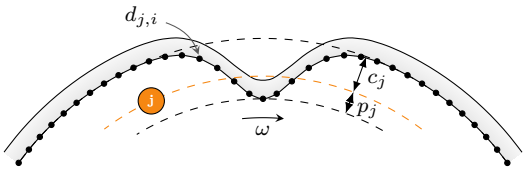

Figure 3 – Casing distortion (▭) in front of the j-th boundary node (●).

3.4 Rubbing event

Whenever a penetration is detected, normal contact forces in the radial direction $\boldsymbol{f}_{3j-2,i}$, see Eq. (15), are computed with the regularized penalty law given in Eq. (31) with $\kappa = 10^9$ N·m^{-1} and $\gamma = 600$ N. In the tangential and axial directions, dry friction forces are accounted for with the Coulomb law where μ corresponds to the friction coefficient. Due to the very high relative speed between the blade-tip and the casing contact surface, it must be underlined that permanent sliding is assumed at all time. Circumferential $\boldsymbol{f}_{3j-1,i}$ and axial $\boldsymbol{f}_{3j,i}$ friction forces components may thus be respectively written as:

$$f_{3j-1,i} = \mu \frac{\dot{x}_{3j-1,i} + \rho_j \omega}{\sqrt{\left(\dot{x}_{3j-1,i} + \rho_j \omega\right)^2 + \dot{x}_{3j,i}^2}} f_{3j-2,i} \tag{37}$$

and:

$$f_{3j,i} = \mu \frac{\dot{x}_{3j,i}}{\sqrt{\left(\dot{x}_{3j-1,i} + \rho_j \omega\right)^2 + \dot{x}_{3j,i}^2}} f_{3j-2,i} \tag{38}$$

for $j \in [\![1..n_b]\!]$, $i \in [\![0..N-1]\!]$ and where ρ_j is the radial position associated to the j-th boundary node. The friction coefficient is set to $\mu = 0.15$.

4 Numerical results

Results obtained using a previously published time integration numerical strategy [23] are presented in the first sub-section. Because this numerical strategy has been successfully applied for the numerical prediction of experimentally witnessed blade-tip/casing contact interactions [4], these results will serve as a reference point in the following sub-sections. It should be underlined that the methodology proposed in this article thus fundamentally differs from the reference time integration numerical strategy both in terms of solution paradigm (frequency method *vs.* time integration) and in terms of contact treatment algorithm (regularized penalty approach *vs.* Lagrange multipliers).

4.1 Reference time integration results

As a first approximation, centrifugal effects are here neglected. Time integration (TI) simulations are carried out at constant angular speed, independently from one another and considering null initial conditions: the blade is initially at rest in the rotating frame. Each simulation is run over 250 blade revolutions for $\omega \in [1\,250,\ 1\,550]$ rad·s^{-1}. All simulations reach a steady state and a Fast Fourier Transform (FFT) of the blade's leading edge radial displacement $\boldsymbol{r}_1(t)$ is computed over the last 50 revolutions. Put side by side, the spectra obtained for each simulation yield the so-called interaction map depicted in Fig. 4a. This interaction map uses a color code (white for lowest amplitudes and black for highest amplitudes) to represent the spectra alongside with even engine orders (- - -) and frequency lines (——). Because the casing features two symmetrical contact lobes, it is evidenced that the frequency content is mostly located along even engine order lines. There are some exceptions however, such as over $\omega \in [1\,500,\ 1\,530]$ rad·s^{-1}. Though an in-depth investigation of this angular speed range goes beyond the scope of this paper, predicted solutions in this area are periodic with a period equivalent to 13.5 blade revolutions. Finally, the location of the linear resonance related to the intersection between the first bending mode and the fourth engine order is evidenced with a red dot (●). The actual location of this resonance—shifted towards higher angular speeds due to the contact stiffening phenomenon—as predicted by the time integration numerical strategy is highlighted with a red triangle (▲).

The jump in the amplitude in the vicinity of the nonlinear resonance appears more clearly when looking at the maximum absolute value—*i.e.* the infinity norm—of the blade's leading edge radial displacement, see Fig. 4b featuring both reference results with Lagrange multipliers (——) and regularized penalty (- - -). This plot underlines the blade's sophisticated dynamics throughout the angular speed range of interest as several jumps of amplitude can be observed. This is strong evidence to indicate that the considered system features co-existing solutions. Because

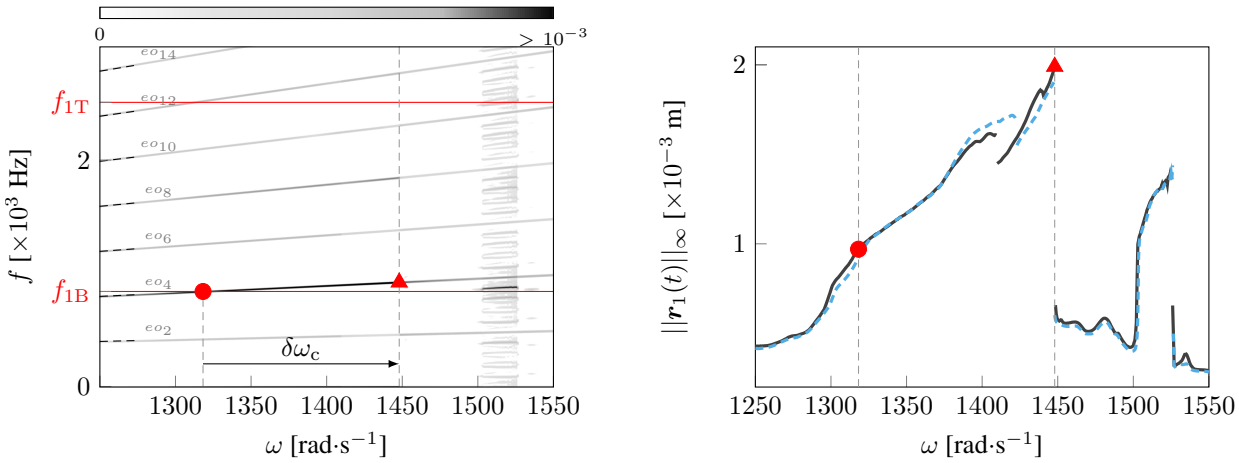

(a) Interaction map

(b) Nonlinear frequency response curve

Figure 4 – TI reference results with Lagrange multipliers (——) and regularized penalty (- - -).

the time integration strategy, as employed here, can only provide a single solution per angular speed, there is no certainty that the nonlinear resonance is accurately predicted: there could exist solutions of higher amplitudes that the time integrator fails to capture with null initial conditions. This is a key motivation for developing a qualitative methodology for the analysis of blade-tip/casing contacts.

4.2 Qualitative analysis of the interaction

Validation of the proposed methodology

The regularized-filtered HBM methods are hereafter referred to as R(F/L/RC)-HBM depending on the employed filtering technique (F: Fejér / L: Lanczos / RC: Raised Cosine), with $H = 40$ and $N = 1024$. The corresponding NFRC are plotted in Fig. 5a. Without filtering, the solver cannot converge, or has visible difficulties to converge over the considered angular speed range. To the contrary, the solver converges with any filtering technique. However,

it is found that the Lanczos filtering procedure (——) provides the most accurate results. In addition to the linear resonance (●) and the TI predicted nonlinear resonance (▲), the nonlinear resonance predicted by the RL-HBM is shown with a diamond symbol (♦). The representation of the solutions of higher amplitudes on an interaction map, see Fig. 5b, highlights the difference between TI and RL-HBM as the contact stiffening phenomenon predicted with RL-HBM ($\delta\omega_{\mathrm{c,HB}} = 209$ rad·s^{-1}) is 61 % higher than the contact stiffening phenomenon predicted by TI ($\delta\omega_{\mathrm{c}} = 130$ rad·s^{-1}). Overall, there is a very good agreement between TI and RL-HBM results. The only significant discrepancy between the two methodologies can be found over the angular speed range $\omega \in [1\,500,\ 1\,530]$ rad·s^{-1}. This is not surprising since, as mentioned above, TI solutions in this area are $13.5\,T$-periodic, which implies that they cannot be captured with the assumed harmonic content of RL-HBM solutions. While it is theoretically conceivable to capture $13.5\,T$-periodic solutions with RL-HBM, this would come at a very high computational cost. Everywhere else, TI and RL-HBM solutions are very similar, both in terms of amplitudes, displacements, contact forces and stresses within the blade (these quantities are not depicted here for the sake of brevity). More importantly, as it will be shown in the following, solutions of higher amplitude, such as the nonlinear resonance predicted with RL-HBM, can be obtained with TI when applying specific initial conditions obtained from the RL-HBM solution.

Performance analysis

In order to quantify the influence of filtering techniques on the convergence of the solver, the density of solution points on the NFRC obtained with R-HBM and RL-HBM for $H = 80$ are plotted in Fig. 6. Each NFRC is subdivided into 80 segments of equal length which are colored according to the number of solution points they contain. Lanczos filtering allows to reduce the number of solutions near turning points (up to −41 % for the first turning point at $\omega = 1425$ rad·s^{-1}). Overall, filtering yields a 15 % decrease of the total number of solution points required to draw the NFRC. These results indicate that filtering may both reduce AFT-induced aliasing [15] and mitigate the Gibbs phenomenon.

Partial conclusion

In the end, it is worth mentioning that the similarity of the results obtained with TI and RL-HBM, as well as the fact that RL-HBM results can be found when using specific initial conditions in TI, seems quite remarkable in a context where the contact management algorithms between the two methodologies are truly different. When developing RL-HBM, initial expectations were that a regularized penalty approach might only provide partially acceptable results over a wide angular speed range. Instead, it is found that the regularized contact law performs very well throughout the angular speed range.

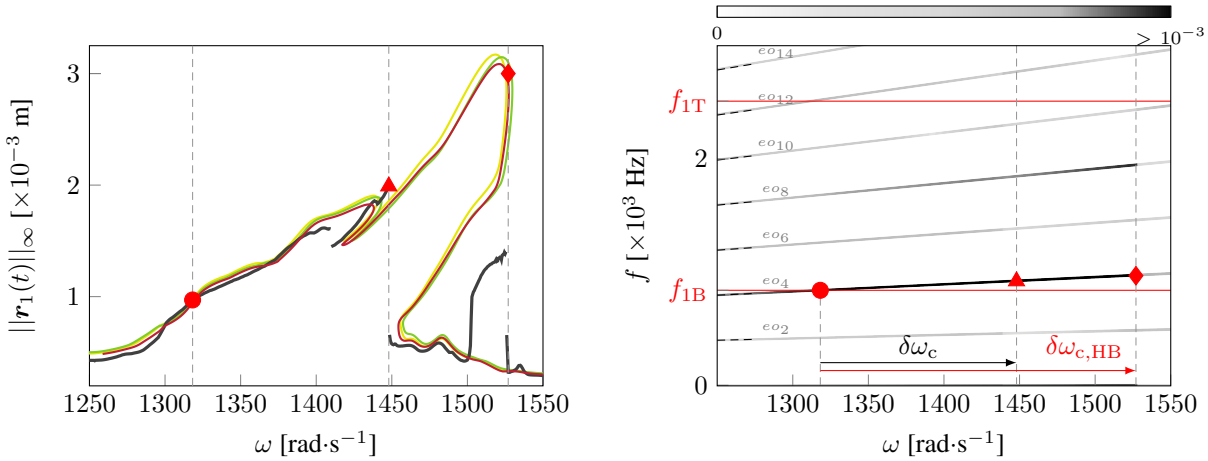

(a) Nonlinear frequency response curve

(b) Interaction map from RL-HBM

Figure 5 – RL-HBM (——), RF-HBM (——) and RRC-HBM (——).

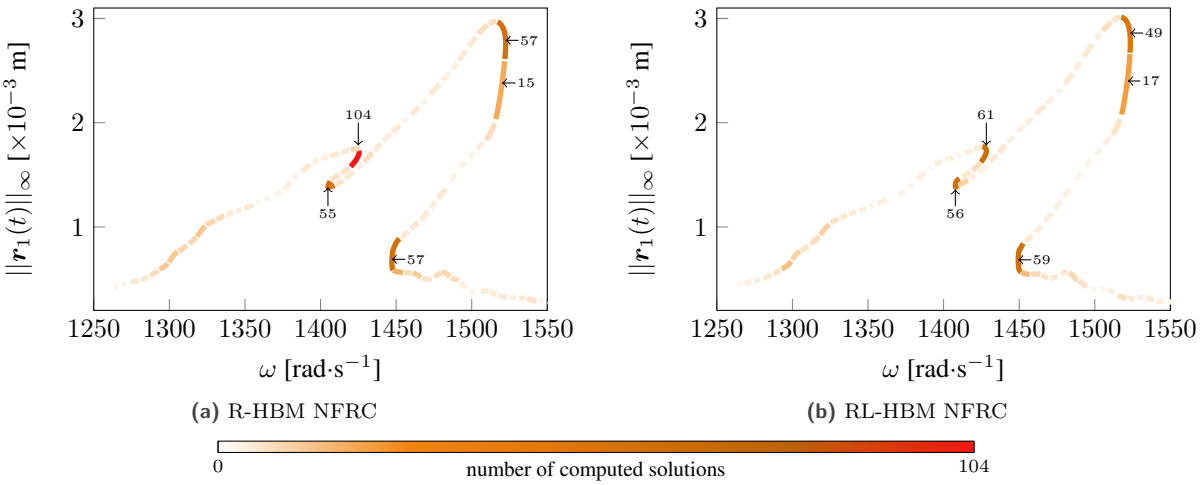

(a) R-HBM NFRC **(b)** RL-HBM NFRC

Figure 6 – Density of solutions ($H = 80$).

The development of RL-HBM paves the way for a more qualitative understanding of blade-tip/casing contact interactions. In particular, the possibility of accurately predicting the nonlinear resonance location may help engineers to design blades more robust to contact interactions. In order to demonstrate the robustness of RL-HBM, the next sub-sections focus on parametric investigations of a few key numerical parameters such as the initial blade/casing clearance, the amplitude of the casing radial distortion, and the value of the blade's modal damping coefficient.

4.3 Parametric investigations

In this section, the NFRC plotted in Fig. 5a is the reference point for all parameter variations; it is plotted in red (——) while the NFRC obtained with variations of a given parameter appear in shades of orange (——)/(——). Reference TI results are also plotted using markers in all the following figures on top of the reference NFRC. For each new set of parameters, in order to avoid too visually dense graphs, only a limited number of TI simulations were run using the RL-HBM solution as initial conditions. The agreement between TI and RL-HBM seen in Fig. 5a is representative of the agreement between the two methodologies for any set of parameters.

Blade-tip/casing clearance is a key quantity for the analysis of blade-tip/casing contact interactions. It is indeed with the intent of minimizing this quantity that manufacturers are invested in better understanding blade-tip/casing contact interactions. Over the past years, it has been shown that operating clearances may significantly affect the blade's dynamics, and that a minor change in this quantity could, from a numerical standpoint, lead to significant variations of the blade's amplitudes of vibration. It has also been underlined that the idea of mitigating hazardous interactions related to contact through an increase of operating clearances may be counter-productive as larger clearances also mean that the blade has more room to vibrate so that blade-tip/casing interactions with greater clearances may be even more detrimental for the blade's amplitudes of vibration. In this study, RL-HBM is used for clearances (that are assumed equal from the leading edge to the trailing edge) varying between $2.5 \cdot 10^{-4}$ m and $12.5 \cdot 10^{-4}$ m. Results obtained for each configuration are plotted in Fig. 7a. There is, overall, a very significant influence of the clearance c_j over the blade's dynamics. The smaller the clearance, the lower the amplitudes of vibrations. However, smaller clearances also very significantly increase the nonlinear resonance frequency of the system. Interestingly, on average, the maximal amplitude of vibration of the blade is found to be between 5 to 6 times higher than the clearance so that the ratio between the maximal amplitude of vibration and c_j remains constant for all considered configurations.

The second parametric investigation focuses on parameter p_j, which defines the radial amplitude of the casing distortion, see Fig. 3. To the best of the author's knowledge, the influence of this parameter has never been

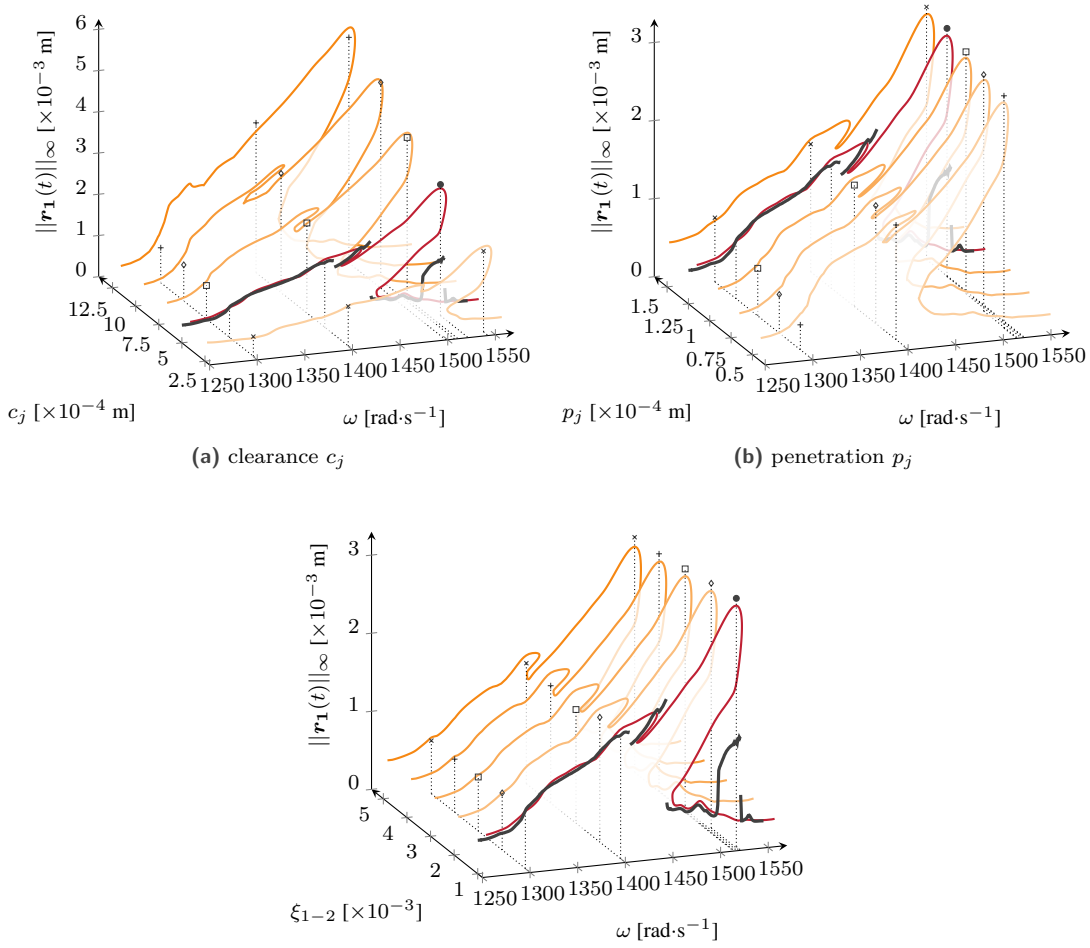

(a) clearance c_j

(b) penetration p_j

(c) damping coefficient ξ_{1-2}

Figure 7 – Variation of c_j, p_j and ξ_{1-2} and related NFRC.

investigated in the literature. Results obtained with the RL-HBM are depicted in Fig. 7b for p_j varying between $0.5 \cdot 10^{-4}$ m and $1.5 \cdot 10^{-4}$ m. Over the considered range of variation of this parameter, there is limited influence over the NFRC which are very much alike for all values of p_j. This is actually an important result since p_j may be seen as a purely numerical parameter that is extremely difficult to calibrate based on experimental data. The minor increase of the nonlinear resonance location as p_j increases seems consistent with the fact that a higher value of p_j implies a more severe contact configuration.

It should also be emphasized that when trying to numerically predict experimentally observed interactions, the definition of a blade's modal damping is arduous. For industrial models, assuming the modal properties are not hidden for confidentiality reasons, it is rarely possible to have meaningful modal damping coefficients for free-vibration modes beyond the first torsional mode. As a consequence, researchers frequently rely on approximated data and often consider a single modal damping coefficient for all modes. In the present study, the modal coefficient of the first two modes (first bending and first torsional modes) ξ_{1-2} varies between 10^{-3} and $5 \cdot 10^{-3}$. All other modes feature a damping coefficient $\xi_{3+} = 5 \cdot 10^{-3}$. The variation of parameter ξ_{1-2} yields the NFRC depicted in Fig. 7c. It is patent that ξ_{1-2} has practically no impact on the RL-HBM results.

Finally, in order to better underline the quality of the results obtained with RL-HBM, as well as their good

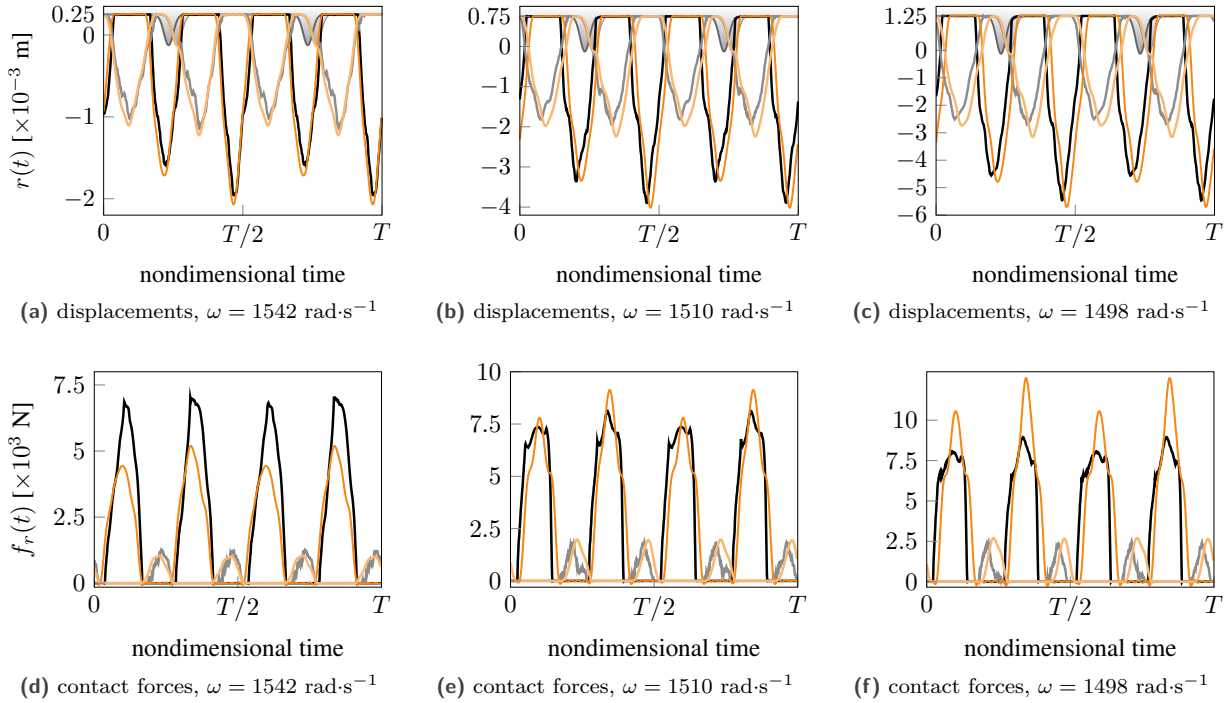

(a) displacements, $\omega = 1542$ rad·s^{-1} **(b)** displacements, $\omega = 1510$ rad·s^{-1} **(c)** displacements, $\omega = 1498$ rad·s^{-1}

(d) contact forces, $\omega = 1542$ rad·s^{-1} **(e)** contact forces, $\omega = 1510$ rad·s^{-1} **(f)** contact forces, $\omega = 1498$ rad·s^{-1}

Figure 8 – Comparison between RL-HBM and TI results obtained at the leading edge (——) (——) and the trailing edge (——) (——) for $c_j = 2.5 \cdot 10^{-4}$ (a)(d), $c_j = 7.5 \cdot 10^{-4}$ (b)(e) and $c_j = 12.5 \cdot 10^{-4}$ (c)(f). Distorted casing (□).

agreement with TI results, the time responses of RL-HBM and TI solutions over one revolution are depicted in Fig. 8. More precisely, the compared solutions correspond to the nonlinear resonances predicted in Fig. 7a for $c_j = 2.5 \cdot 10^{-4}$ m, $c_j = 7.5 \cdot 10^{-4}$ m and $c_j = 12.5 \cdot 10^{-4}$ m. The comparison of TI and RL-HBM solutions in the vicinity of nonlinear resonances is motivated by the fact that this is an area where non negligible variations of amplitudes are found and it seems relevant to ensure that this does not translate into significant differences in the time domain. As a reminder, TI solutions in this area could not be obtained with null initial conditions, they are here obtained using the RL-HBM solution as initial conditions.

There is an excellent agreement between TI and RL-HBM solutions in terms of displacements, both at the leading edge and the trailing edge, see Figs. 8a, 8b and 8c. Though this is not shown for clarity, it has been checked that there is also an excellent agreement on the axial, tangential, and radial displacements of all other contact nodes. One may also notice no visible spurious oscillations of the RL-HBM solutions close to contact areas. On the contrary, very small oscillations may be found on the contact forces computed with RL-HBM. The very small amplitude of these oscillations underlines the suitability of the Lanczos filtering technique. Interestingly, there are non negligible differences on the contact forces between TI and RL-HBM. Because these differences do not translate into significant differences in terms of displacements, they are assumed to be related to the two different types of contact treatment procedures employed in TI and RL-HBM.

4.4 Accounting for centrifugal effects

In order to increase the fidelity of the considered mechanical system, this section focuses on accounting for centrifugal effects. With respect to the considered mechanical system, the influence of centrifugal effects is twofold: (1) on the one hand, the stiffness matrix of the blade becomes dependent on the angular speed ω, and (2) on the other hand, centrifugal effects also imply a small deformation of the blade so that the blade-tip/casing clearance configuration also depends on ω.

In this study, the influence of centrifugal effects is limited to the dependence of the stiffness matrix to the angular speed ω. The focus on the variation of the stiffness matrix alone is motivated by the fact that the influence of blade-tip/casing clearances was looked at in the previous section. However, there would be absolutely no issue to account for the influence of centrifugal effects on blade-tip/casing clearances with RL-HBM.

It has been shown in the literature [27] that, when accounting for centrifugal effects over the angular speed range $\omega \in [0,\ \omega_{\max}]$, the blade's stiffness matrix may be written as follows:

$$\mathbf{K}(\omega) = \mathbf{K}_0 + \mathbf{K}_1\omega^2 + \mathbf{K}_2\omega^4 \tag{39}$$

where the matrices $\mathbf{K}_0$, $\mathbf{K}_1$ and $\mathbf{K}_2$ are obtained from linear combination of stiffness matrices computed at $\omega = 0$, $\omega = \omega_{\max}/2$ and $\omega = \omega_{\max}$. Transferring this polynomial development within a reduced space—which is required for efficient computations—requires to enrich the Craig-Bampton reduction basis with constrained and clamped modes computed at these same three angular speeds, thus yielding a reduced-order model with three times more dof: $n = 102 = 3 \times 34$ for the considered blade.

In the context of the HBM, the matrix $\mathbf{Z}(\omega)$ from Eq. (6) must be rewritten accordingly. Its derivative counterpart $\mathbf{Z}_{,\omega}$ with respect to ω in Eq. (14) becomes:

$$\mathbf{Z}_{,\omega} = 2\omega\nabla^2 \otimes \mathbf{M} + \nabla \otimes \mathbf{C} + \mathbf{I}_{2H+1} \otimes \left(2\omega\mathbf{K}_1 + 4\omega^3\mathbf{K}_2\right) \tag{40}$$

The NFRC obtained with centrifugal effects (——) are depicted in Figs. 9a and 9b, respectively looking at the infinity norm of the blade's leading edge radial displacement and the blade's trailing edge radial displacement. Previous results obtained without centrifugal effects (——) are plotted on the same figures to ease comparison between the plots. In both cases, corresponding TI results with null initial conditions are plotted in black (——) and the amplitude of the TI solution obtained at the nonlinear resonance taking the RL-HBM solution as initial conditions is marked by a black dot (●).

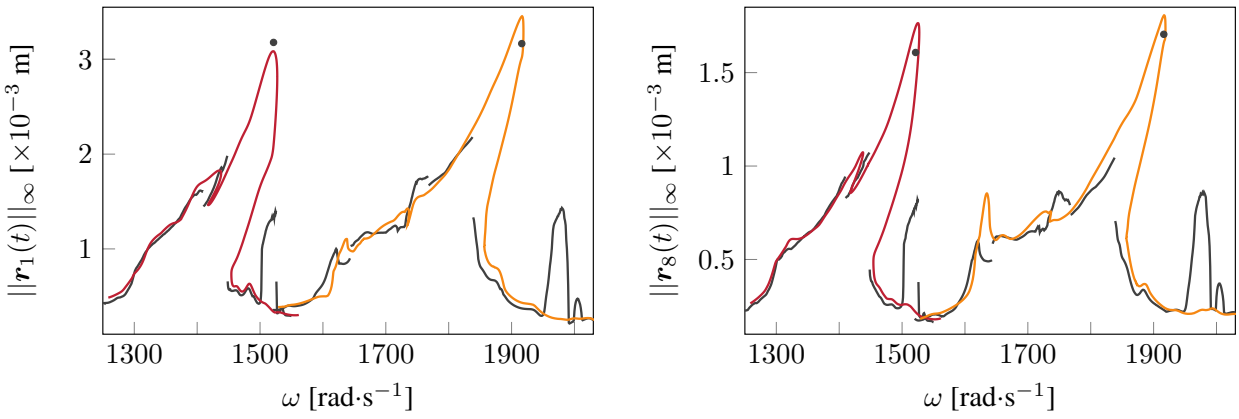

(a) Leading edge **(b)** Trailing edge

Figure 9 – Comparison between RL-HBM and TI results with (——) and without (——) centrifugal effects.

The eigenfrequency of the first bending mode significantly increases with the angular speed ω when centrifugal effects are accounted for. For that reason, the angular speed range over which the first eigenfrequency of the blade intersects the fourth engine order line is shifted and the nonlinear resonance is now predicted at $\omega = 1\,916$ rad·s^{-1}. The increase of the blade's first eigenfrequency also implies a greater proximity between this frequency line and the fourth engine order line, visible in the interaction map—obtained with TI—drawn in Fig. 10. This explains that the angular speed range over which higher amplitudes of vibration are predicted is wider with centrifugal effects: $\omega \in [1\,620,\ 1\,916]$ rad·s^{-1}, to be compared with the range $\omega \in [1\,300,\ 1\,530]$ rad·s^{-1} without centrifugal effects.

Overall, there is still a very good agreement between TI results and RL-HBM. It is noticeable however that there are more areas over which minor differences arise. This is related to the very sophisticated behaviour of TI

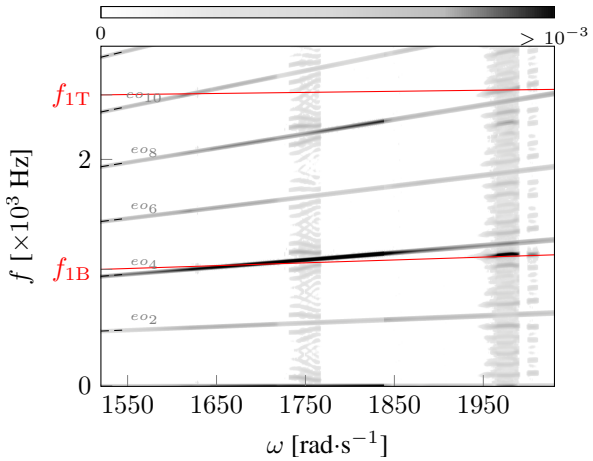

Figure 10 – Interaction map with centrifugal effects obtained at the leading edge (TI simulations).

results (dense harmonic content) around $\omega = 1\,750$ rad·s^{-1}. Also, $13.5\,T$-periodic solutions are still predicted below $\omega = 2\,000$ rad·s^{-1}.

Finally, in terms of calculation times, RL-HBM approach is found to be very efficient: about 22 minutes are required to compute the NFRC pictured in Fig. 5a on a standard PC (i7 processor 7700K 4.2 GHz). This is about 20 times faster than the computation times required for TI simulations. Nevertheless, while TI simulations relied on an optimized Python/Numba code, it is estimated that TI computation times could still be lowered significantly through the implementation of an auto-correlation procedure for the detection of steady state. For this reason, the gain from TI to RL-HBM may be here slightly over-estimated.

5 Conclusion

This paper introduces a Harmonic Balance Method-based methodology for the qualitative analysis of blade-tip/casing contact interactions in aircraft engines. It is applied to an open case study based on NASA rotor 37. An in-depth comparison of the obtained results with those of a reference time integration numerical strategy underlines the suitability of the proposed approach and its ability to accurately predict the blade's nonlinear resonance. The proposed methodology does not yield any modelling restriction with respect to the reference numerical strategy: it can account for a large number of boundary nodes, friction, centrifugal effects as well as any type of casing distortion. In the end, the presented results highlight that time integration approaches and frequency methods complement each other since the observation of very sophisticated vibration behaviours—such as the predicted $13.5\,T$-periodic solutions—cannot yet be efficiently obtained with frequency methods. Conversely, time integration methods are unable to efficiently predict nonlinear resonances.

Acknowledgment

This research was supported by the Natural Sciences and Engineering Research Council of Canada (NSERC).

References

[1] Padova, C., Barton, J., Dunn, M. G., and Manwaring, S., 2006. "Experimental results from controlled blade tip/shroud rubs at engine speed". *J. Turbomach.,* **129**(4), pp. 713–723. doi: 10.1115/1.2720869 - oai: hal-01333702v1.

[2] Millecamps, A., Brunel, J.-F., Dufrénoy, P., Garcin, F., and Nucci, M., 2009. "Influence of thermal effects during blade-casing contact experiments". In Proceedings of the ASME IDETC/CIE 2009, pp. 855–862. doi: 10.1115/DETC2009-86842 - oai: hal-01223060.

[3] Nyssen, F., Tableau, N., Lavazec, D., and Batailly, A., 2020. "Experimental and numerical characterization of a ceramic matrix composite shroud segment under impact loading". *J. Sound Vib.,* **467**, p. 115040. doi: 10.1016/j.jsv.2019.115040 - oai: hal-02378746.

[4] Batailly, A., Legrand, M., Millecamps, A., and Garcin, F., 2012. "Numerical-experimental comparison in the simulation of rotor/stator interaction through blade-tip/abradable coating contact". *J. Eng. Gas Turbines Power,* **134**(8), p. 11. doi: 10.1115/1.4006446 - oai: hal-00746632.

[5] Almeida, P., Gibert, C., Thouverez, F., Leblanc, X., and Ousty, J.-P., 2016. "Numerical analysis of bladed disk–casing contact with friction and wear". *J. Eng. Gas Turbines Power,* **138**(12), p. 11. doi: 10.1115/1.4033065.

[6] Thorin, A., Guérin, N., Legrand, M., Thouverez, F., and Almeida, P., 2018. "Nonsmooth Thermoelastic Simulations of Blade–Casing Contact Interactions". *J. Eng. Gas Turbines Power,* **141**(2), p. 7. doi: 10.1115/1.4040857 - oai: hal-01989188.

[7] Meingast, M. B., Legrand, M., and Pierre, C., 2014. "A linear complementarity problem formulation for periodic solutions to unilateral contact problems". *Int. J. Non-Linear Mech.,* **66**, pp. 18–27. doi: 10.1016/j.ijnonlinmec.2014.01.007 - oai: hal-00955647v1.

[8] Von Groll, G., and Ewins, D. J., 2001. "The harmonic balance method with arc-length continuation in rotor/stator contact problems". *J. Sound Vib.,* **241**(2), pp. 223–233. doi: 10.1006/jsvi.2000.3298 - oai: hal-01333704.

[9] Nacivet, S., Pierre, C., Thouverez, F., and Jezequel, L., 2003. "A dynamic Lagrangian frequency–time method for the vibration of dry-friction-damped systems". *J. Sound Vib.,* **265**(1), pp. 201–219. doi: 10.1016/S0022-460X(02)01447-5 - oai: hal-01635272.

[10] Krack, M., Panning-von Scheidt, L., and Wallaschek, J., 2016. "On the interaction of multiple traveling wave modes in the flutter vibrations of friction-damped tuned bladed disks". *J. Eng. Gas Turbines Power,* **139**(4), p. 9. doi: 10.1115/1.4034650.

[11] Krack, M., Salles, L., and Thouverez, F., 2017. "Vibration prediction of bladed disks coupled by friction joints". *Arch. Comput. Methods Eng.,* **24**(3), pp. 589–636. doi: 10.1007/s11831-016-9183-2 - oai: hal-01825517.

[12] Petrov, E. P., 2012. "Multiharmonic analysis of nonlinear whole engine dynamics with bladed disc-casing rubbing contacts". In Proceedings of the ASME Turbo Expo 2012, Vol. Volume 7: Structures and Dynamics, Parts A and B, pp. 1181–1191. doi: 10.1115/GT2012-68474.

[13] Jerri, A. J., 1998. *The Gibbs Phenomenon in Fourier Analysis, Splines and Wavelet Approximations*, Vol. 446. Springer, Boston, MA. doi: 10.1007/978-1-4757-2847-7.

[14] Krack, M., and Gross, J., 2019. *Harmonic Balance for Nonlinear Vibration Problems*. Springer, Cham. doi: 10.1007/978-3-030-14023-6.

[15] Woiwode, L., Narayanaa Balaji, N., Kappauf, J., Tubita, F., Guillot, L., Vergez, C., Cochelin, B., Grolet, A., and Krack, M., 2020. "Comparison of two algorithms for harmonic balance and path continuation". *Mech. Syst. Signal Process.,* **136**, p. 106503. doi: 10.1016/j.ymssp.2019.106503 - oai: hal-02424746.

[16] Keller, H. B., 1983. "The bordering algorithm and path following near singular points of higher nullity". *SIAM J. Sci. and Stat. Comput.,* **4**(4), pp. 573–582. doi: 10.1137/0904039.

[17] Cameron, T. M., and Griffin, J. H., 1989. "An alternating frequency/time domain method for calculating the steady-state response of nonlinear dynamic systems". *J. Appl. Mech.,* **56**(1), pp. 149–154. doi: 10.1115/1.3176036 - oai: hal-01333697.

[18] Narayanan, S., and Sekar, P., 1998. "A frequency domain based numeric–analytical method for non-linear dynamical systems". *J. Sound Vib.,* **211**(3), pp. 409–424. doi: 10.1006/jsvi.1997.1319.

[19] Cardona, A., Lerusse, A., and Géradin, M., 1998. "Fast Fourier nonlinear vibration analysis". *Comput. Mech.,* **22**(2), pp. 128–142. doi: 10.1007/s004660050347.

[20] Sarrouy, E., and Sinou, J.-J., 2011. "Non-linear periodic and quasi-periodic vibrations in mechanical systems - on the use of the harmonic balance methods". In *Advances in Vibration Analysis Research*, F. Ebrahimi, ed. IntechOpen, Rijeka, ch. 21, pp. 419–434. doi: 10.5772/15638 - oai: hal-00730895.

[21] Djeddi, R., and Ekici, K., 2016. "Resolution of gibbs phenomenon using a modified pseudo-spectral operator in harmonic balance cfd solvers". *Int. J. Comput. Fluid Dyn.,* **30**(7-10), pp. 495–515. doi: 10.1080/10618562.2016.1242726.

[22] Reid, L., and Moore, R. D. Design and overall performance of four highly loaded, high speed inlet stages for an advanced high-pressure-ratio core compressor. Tech. rep., NASA Lewis Research Center Cleveland, OH, United States. https://ntrs.nasa.gov/citations/19780025165, 1978 (accessed 2020-10-29).

[23] Piollet, E., Nyssen, F., and Batailly, A., 2019. "Blade/casing rubbing interactions in aircraft engines: Numerical benchmark and design guidelines based on nasa rotor 37". *J. Sound Vib.,* **460**, p. 114878. doi: 10.1016/j.jsv.2019.114878 - oai: hal-02281666.

[24] Craig Jr, R. R., and Bampton, M. C. C., 1968. "Coupling of substructures for dynamic analyses". *AIAA J.,* **6**(7), pp. 1313–1319. doi: 10.2514/3.4741.

[25] Batailly, A., Legrand, M., Cartraud, P., and Pierre, C., 2010. "Assessment of reduced models for the detection of modal interaction through rotor stator contacts". *J. Sound Vib.,* **329**(26), pp. 5546–5562. doi: 10.1016/j.jsv.2010.07.018 - oai: hal-00524762v1.

[26] Huebler, D. Rotor 37 and stator 37 assembly. Records of the National Aeronautics and Space Administration, 1903 - 2006. Photographs relating to agency activities, facilities and personnel, 1973 - 2013. https://catalog.archives.gov/id/17468361, 1977 (accessed 2020-10-29).

[27] Sternchüss, A., and Balmès, E., 2006. "On the reduction of quasi-cyclic disk models with variable rotation speeds". In Proceedings of the Int. Conference on Adv. Acoustics and Vib. Eng., pp. 3925–3939. oai:hal-00266394.